Journal of
Marine Science and Engineering

MDPI

Article

On the Compression Instability during Static and Low-Cycle Fatigue Loadings of AA 5083 Welded Joints: Full-Field and Numerical Analyses

Pasqualino Corigliano

Department of Engineering, University of Messina, 98166 Messina, Italy; pcorigliano@unime.it

Abstract: The aim of this scientific work was to evaluate the compression instability effects during static and low-cycle fatigue loadings of AA 5083 welded joints, commonly used in marine structures. Low-cycle fatigue assessment in marine structures is of utmost importance since high levels of plastic deformation can arise in the proximity of high-stress concentration areas. Displacement ratios equal to minus one and zero were used to perform experimental low-cycle fatigue tests. The tests were monitored by means of the Digital Image Correlation technique in order to detect the strain patterns, with particular attention paid to stress concentration areas, indicating that a specimen tends to buckle during high compression loads, for tests with a displacement ratio of minus one. The tests at displacement ratios equal to −1 showed a lowering of the strain–life curve revealing a considerable effect on compression instability. A nonlinear finite element modelling procedure, depending only on hardness measurements, was developed. The hardness measurements were used in order to assess the distinct mechanical properties of the different zones that were included in the finite element model. The finite element model results were compared to the data achieved by means of the digital image correlation technique, demonstrating that hardness measurements can help predict the low-cycle fatigue behaviour of welded joints and consider compression instability phenomena.

Keywords: low-cycle fatigue; marine structures; digital image correlation; welded joints; finite element analysis; compression instability

Citation: Corigliano, P. On the Compression Instability during Static and Low-Cycle Fatigue Loadings of AA 5083 Welded Joints: Full-Field and Numerical Analyses. *J. Mar. Sci. Eng.* **2022**, *10*, 212. https://doi.org/10.3390/jmse10020212

Academic Editor: José A.F.O. Correia

Received: 28 December 2021
Accepted: 31 January 2022
Published: 5 February 2022

1. Introduction

Most marine structures involve tubular or plate details linked by welded joints with longitudinal and transverse elements that are exposed to severe weather conditions, such as storms, loading/unloading operations, and intense wave loads, which cause significant fatigue loads and cracks [1–7]. Adding these effects to the welding process, which produces variations in local mechanical properties, further complicates the problems. Local mechanical properties are assumed to vary from the base material (BM) to the heat-affected zone (HAZ) and the weld metal (WM) [8]. The thickness effect is also an influencing factor [9].

The stress concentrations, due to the presence of welds under fatigue loadings, induce cyclic stresses that go beyond the yield stress locally. Marine constructions could thus encounter a low-cycle fatigue (LCF) life and plastic deformation accumulation phenomena may appear, causing failures due to fatigue (mainly at welded joints). The corrosion environment, such as seawater, reduces the fatigue strength by roughly fifty percent in steel welded joints [10].

The fatigue assessment of welded joints is extensively studied and many approaches have been developed during recent decades [11]. The simplest approach is nominal stress, since it is not influenced by local stress changes produced by structural discontinuities (i.e., a stiffener end or local weld toe). The hot-spot stress approach [12,13] incorporates all stress effects excluding those caused by the local weld profile. The effective notch stress approach [14,15] also considers the local stress increase at the notch formed by the weld toe

or the weld root, without taking into consideration the elastic-plastic material behaviour. The notch stress intensity factor method [16,17] is mostly applied to evaluate crack initiation at sharp corners and includes the effects of flank angles.

Critical distance approaches [18,19] state that a structure is subjected to fatigue failure when the fatigue limit is reached within a region encompassing the notch (critical length or volume), and not only at a single point. The thermographic method [20–23] assumes that the fatigue limit is intended as the maximum stress during a fatigue test generating no increment of temperature.

The notch strain approach [24] is mainly used for the low-cycle fatigue (LCF) assessment of welded details to contemplate the effect of elastic-plastic stress/strain on material behaviour. However, the cyclic stress/strain curve should be priorly known to achieve accurate non-linear FE simulations.

The traction stress/strain approach [25] neglects the effects of local notch radii and is suitable for the fatigue behaviour of welded structural elements having no defined notch radii [13,25–29]. Key advantages of the structural stress/strain method are that it is not mesh-sensitive, the fatigue data can be incorporated within only one master S-N/E-N curve (i.e., without weld classification approaches), and it works well for both HCF and LCF.

Most of the methods described above are generally applied for high-cycle fatigue failure and fewer for low-cycle fatigue failure (the most common and efficient are the notch strain approach and the equivalent structural strain approach).

As reported, many studies about the fatigue of welded connections exist. However, to the author's knowledge, the instability effects of high compression loadings and how these affect LCF life have not been appropriately considered. High plastic strain develops during LCF loadings, and the material changes should be considered. An interesting study regarding 316 L stainless steel with variable loading paths revealed that the materials exhibited cyclic hardening at the initial stage, followed by a long period of cyclic softening (conducted in [30]). The strain hardening gradient effect on short crack behaviour and a new crack transition length concept to describe short cracks in EH36 joints were proposed in [31].

The aim of this study was to assess and comprehend the LCF behaviour of welded joints made of AA 5086, widely used in marine installations and constructions, considering the effects of high values of applied displacements during the compression phase and how these affect the LCF life.

A procedure was developed that centred on nonlinear finite element analysis (FEA), which required as input only the hardness values of the different zones (BM, HAZ, WM). Experimental low-cycle fatigue tests were performed at two displacement ratios ($R_d = 0$ and $R_d = -1$). Digital image correlation (DIC) was used to analyse the full-field strain patterns to evaluate the presence of instability during compression loadings and to validate the FE model procedure. The author employed the DIC technique to different kinds of connections [32–34].

2. Materials and Methods

The 5000 and 6000 series aluminium alloys are those most widely used in corrosive environments, such as the marine environment. The investigated welded specimens were made of AA 5083, welded by means of the MIG process and provided by a shipyard. Figure 1 shows the geometric dimensions (width of 24.5 mm). The mechanical parameters of the investigated AA 5083 are reported in Table 1.

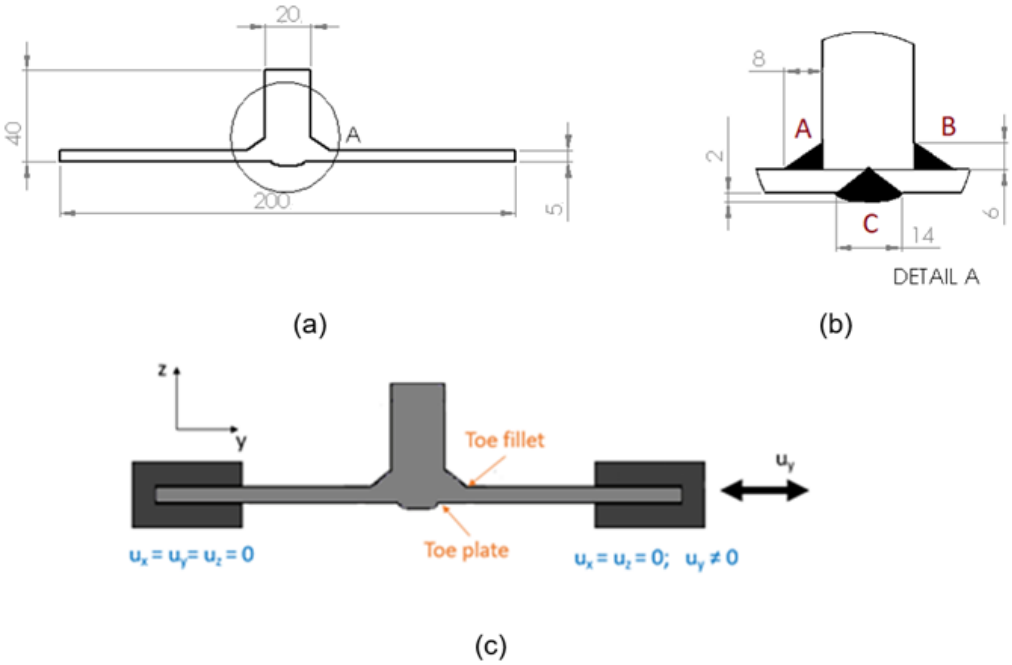

Figure 1. Geometry (**a**), weld details (**b**), boundary and loading conditions (**c**) of welded specimens.

Table 1. Mechanical properties of the investigated Al alloy.

Ultimate Stress, σ_u	Yield Stress, σ_y	Elongation at Break, ε_u	Young's Modulus, E
MPa	**MPa**	**%**	**MPa**
317	228	16	71,000

The specimen surface was polished in order to achieve accurate hardness measurements. The hardness values were taken following a line path from weld A to weld B, then from weld C to weld A at 45 degrees (see Figure 1).

The size of the specimens together with the loading and boundary conditions were the same for static and LCF tests (see Figure 1).

The experimental tests were performed using an 8850 Instron testing machine with a load cell of ±250 kN.

The 3D ARAMIS 12M, supplied by GOM GmbH, was used for 3D DIC analyses with the aim of monitoring stress concentration zones (i.e., weld toes) that cannot be monitored using strain gages. Two 12 megapixel cameras, with a 50 mm focal length, were employed. To perform 3D analysis using the 3D DIC technique, a calibration of the system was needed. A calibration panel (CP 20–175 × 140 mm^2), provided by the producer company and reproducing the measuring volume of the specimens, was used for system calibration [35]. The facet size was set to 12, while the step size was 10. The accuracy of the system was to 0.01% in terms of measured displacements. A black–white speckle pattern was painted on the specimen surface for the DIC evaluations.

The 3D FE nonlinear analyses were performed with ANSYS software. To consider the large deformation effect, the nonlinear geometric option was adopted in the FE analyses. It is known that the local toe radius can vary in each specimen and can be different also in the same plate [36], thus a nominal value of the notch radius of 1 mm was modelled for the FE analyses to avoid stress/strain singularities. Twenty nodes solid elements (SOLID186) and multilinear kinematic hardening were used. SOLID186 is a higher order 3D 20-node solid element. The element is defined by 20 nodes having three degrees of freedom per node: translations in the nodal x, y, and z directions. The number of nodes of the FE model is 297,060, with an element size in the weld toe of 0.1 mm. The mesh was refined following the

IIW recommendations [37]. The non-linear material properties inserted in the FE models, which are different for static and cyclic evaluations, were evaluated based on hardness measurements. The loading and boundary conditions were set with the aim of reproducing the experimental conditions. (See Figure 1c.)

Material Properties as a Funciotn of Hardness Measurements

It is known that the mechanical properties of the base material (BM), heat-affected zone (HAZ) and welded metal (WM) are different, and they can be correlated to hardness values. No hardness differences were observed between BM and HAZ. In this study, the BM and WM were treated as if they were different alloys, related to their properties for hardness measurements. The used relationships for mechanical properties determination (ultimate stress σ_u and yield stress σ_y), which are empirical equations often used for Al alloys and validated in previous studies [38], are reported in Equations (1) and (2):

$$\sigma_u = 2.4079 \cdot HV + 46.39 \quad (1)$$

$$\sigma_y = 2.9263 \cdot HV - 44.289 \quad (2)$$

Table 1 reports the three Vickers hardness values detected. The welded metals (WM) revealed lower values of hardness compared to base material (BM) and heat-affected zones (HAZ). The properties calculated from Equations (1) and (2) are illustrated in Table 2 (welds A, B, and C are shown in Figure 1).

Table 2. Static properties from hardness measurements.

	HV (MPa)	σ_y **(MPa)**	σ_u **(MPa)**
BM and HAZ	91.8	224.3	267.4
WM of welds A and B	74.5	173.7	225.7
WM of weld C	82	195.6	243.8

To perform accurate nonlinear FE analyses, the values of σ_y and σ_u were used to achieve the static true stress–strain curves, based on the Ramberg–Osgood (R-O) equation. The adopted method, developed by Kamaya [39], is centred on the relationships shown in Equations (3)–(5).

$$\frac{E\varepsilon}{\sigma_Y} = \frac{\sigma}{\sigma_Y} + \alpha\left(\frac{\sigma}{\sigma_Y}\right)^m \quad (3)$$

Considering the plastic strain at the yield point $\varepsilon_{pY} = 0.2\%$, α and m are:

$$\alpha = \frac{E\varepsilon_{pY}}{\sigma_Y} \quad (4)$$

$$m = 3.93\left[ln\left(\frac{\sigma_{ut}}{\sigma_Y}\right)\right]^{-0.754} \quad (5)$$

The calculated α and m values are given in Table 3.

Table 3. R-O parameters.

	BM and HAZ	**WM of Welds A, B**	**WM of Weld C**
m	14.6	10.8	12.3
α	0.63	0.82	0.73

The stress–strain curves calculated from Equation (3) are displayed in Figure 2.

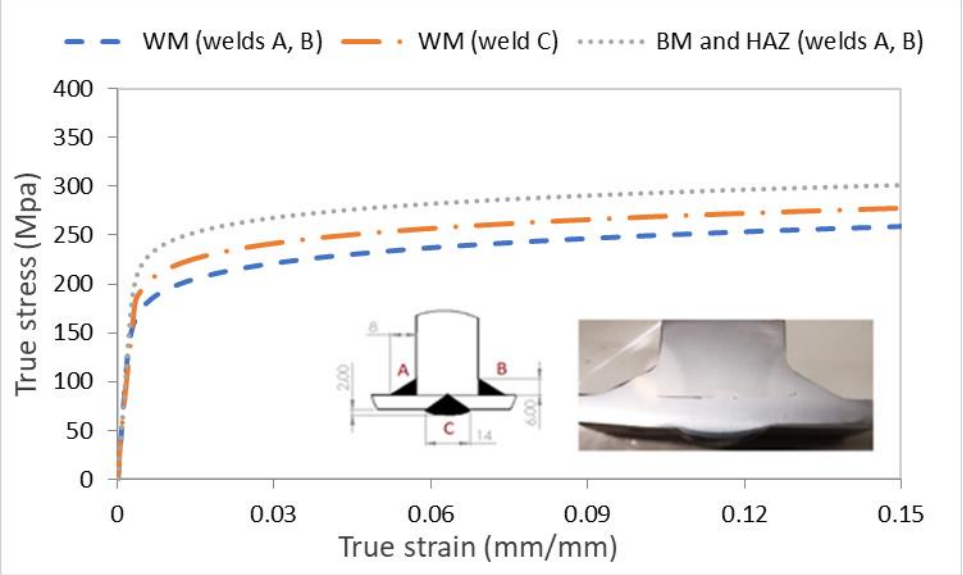

Figure 2. Static stress–strain curves determined based on hardness results.

When dealing with LCF conditions, the stabilized cyclic stress–strain curve needs to be evaluated. The curve is also based on the Ramberg–Osgood equation, as a function of the strain hardening exponent (n') and cyclic strength coefficient (K'):

$$\frac{\Delta\varepsilon}{2} = \frac{\Delta\varepsilon_e}{2} + \frac{\Delta\varepsilon_p}{2} = \frac{\Delta\sigma}{2 \cdot E} + \left(\frac{\Delta\sigma}{2 \cdot K'}\right)^{1/n'} \quad (6)$$

According to Lopez and Fatemi [40], the stabilized cyclic stress–strain curve parameters can be assessed by the calculations reported in Equations (7)–(10).

$$K' = 1.16 \cdot \sigma_u + 593, \text{ for } \frac{\sigma_u}{\sigma_y} > 1.2 \quad (7)$$

$$K' = 3 \cdot 10^{-4} {\sigma_u}^2 + 0.23 \cdot \sigma_u + 619, \text{ for } \frac{\sigma_u}{\sigma_y} \leq 1.2 \quad (8)$$

$$n' = -0.37 \log\left(\frac{0.75 \cdot \sigma_y + 82}{1.16 \cdot \sigma_u + 593}\right) 1.16 \cdot \sigma_u + 593, \text{ for } \frac{\sigma_u}{\sigma_y} > 1.2 \quad (9)$$

$$n' = -0.37 \log\left(\frac{3 \cdot 10^{-4} \cdot {\sigma_y}^2 - 0.15 \cdot \sigma_y + 526}{3 \cdot 10^{-4} \cdot {\sigma_u}^2 - 0.23 \cdot \sigma_u + 619}\right), \text{ for } \frac{\sigma_u}{\sigma_y} \leq 1.2 \quad (10)$$

Given the σ_u/σ_y ratio of the AA 5083 welded joint considered in this study, the cyclic parameters K' and n' were calculated using Equations (7) and (9) and are reported in Table 4. The obtained curves, calculated from Equation (6), are reported in Figure 3.

Table 4. Cyclic R-O parameters.

	σ_y (MPa)	σ_u (MPa)	K' (MPa)	n'
BM and HAZ	224.4	267.4	0.206237	903.2
WM (weld C)	195.7	243.8	0.215732	875.8
WM (welds A, B)	173.7	225.8	0.223842	854.9

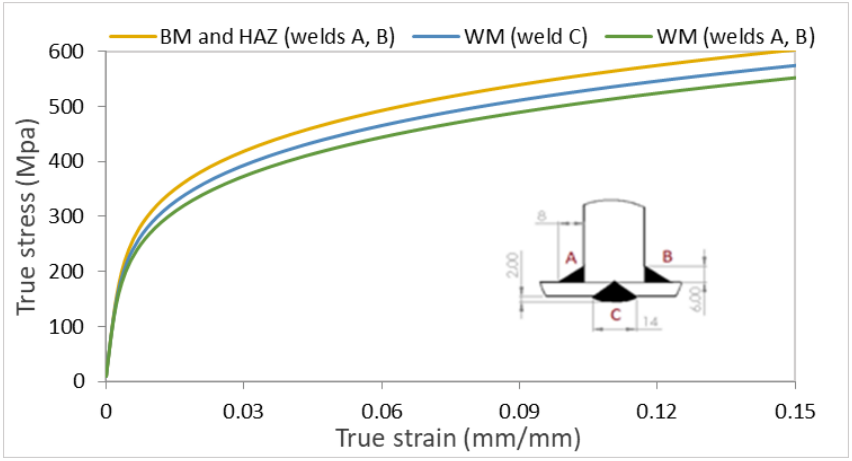

(**a**)

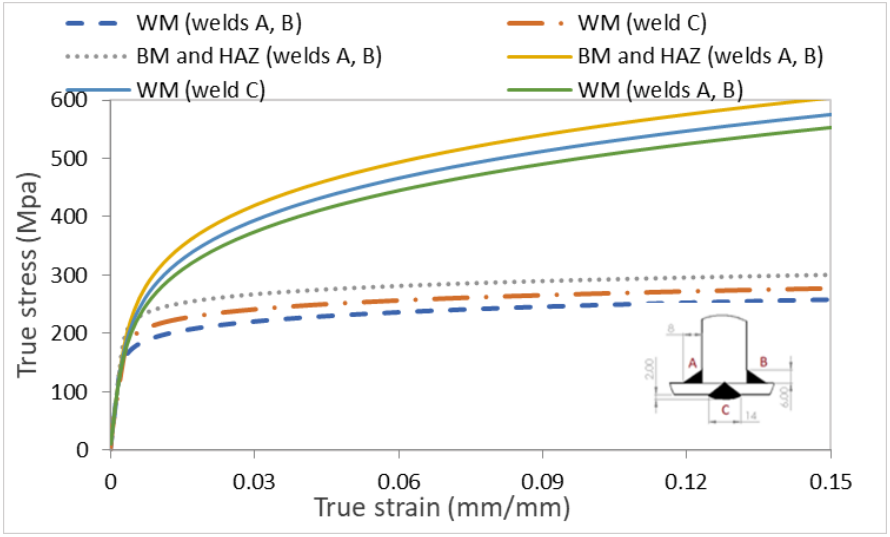

(**b**)

Figure 3. (**a**) Cyclic stress–strain curves calculated with data from hardness test, (**b**) Stress–strain curves from hardness. Static: dotted lines; cyclic: continuous lines.

A comparison of the curves evaluated by hardness measurements is shown in Figure 3b. The figure clearly shows a strain-hardening of the cyclic curve of the three materials' zones, which is typical of this kind of Al alloy (as was reported in [41]).

3. Results from Initial Evaluations

The same size of sample was used for the static tests as was used for the LCF tests. One preliminary static test was performed in order to detect the onset of buckling, in terms of applied displacement. The value of the amplitude displacement (reversed sinusoidal cycle at $R_d = -1$) was equal to $\pm$ 0.45 mm. It must be noted that only one cycle was performed in order to consider the static behaviour before each specimen began to harden. Figure 4 shows the longitudinal strain maps assessed by the DIC technique at maximum and minimum applied displacements. Some detection points (namely Stage Points (SP)) were introduced for the DIC analysis. The distance between two SP was 5 mm.

For both positive and negative applied displacements, the value of the longitudinal strain was always positive for SP4. This was because, during compression loadings, bending occurred and the specimens tended to buckle.

The nonlinear finite element analyses were performed considering the loading and boundary conditions already mentioned and using the nonlinear material curves evaluated from the hardness measurements previously shown in Figure 2.

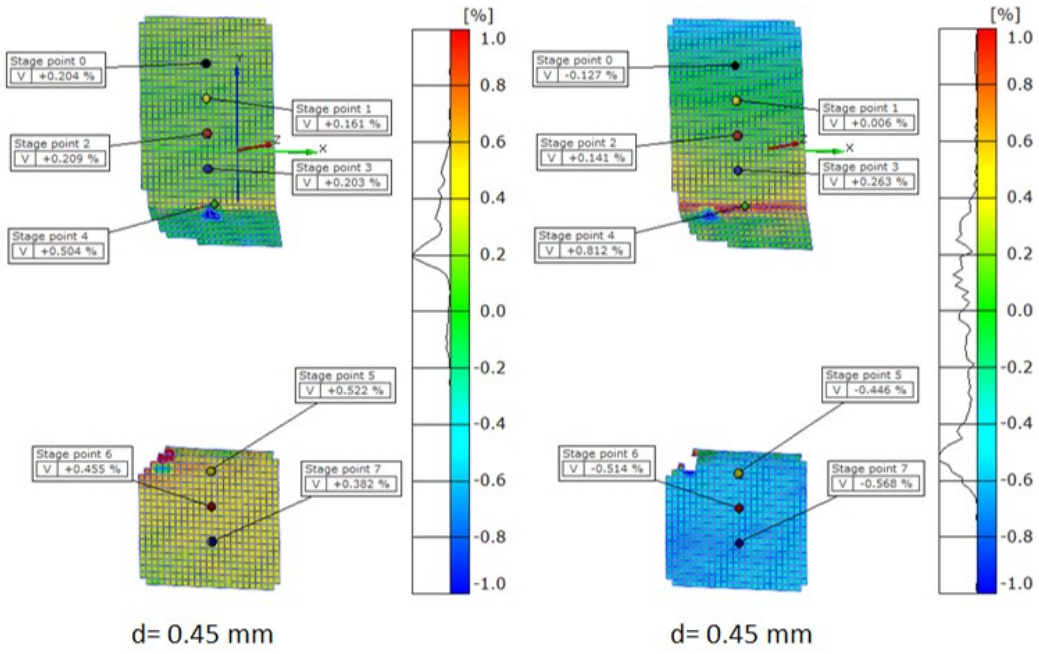

Figure 4. Longitudinal strain maps by means of DIC. ((**Left**) d = 0.45 mm; (**Right**) d = −0.45 mm.)

The FE model and different materials employed in the static analyses are shown in Figure 5.

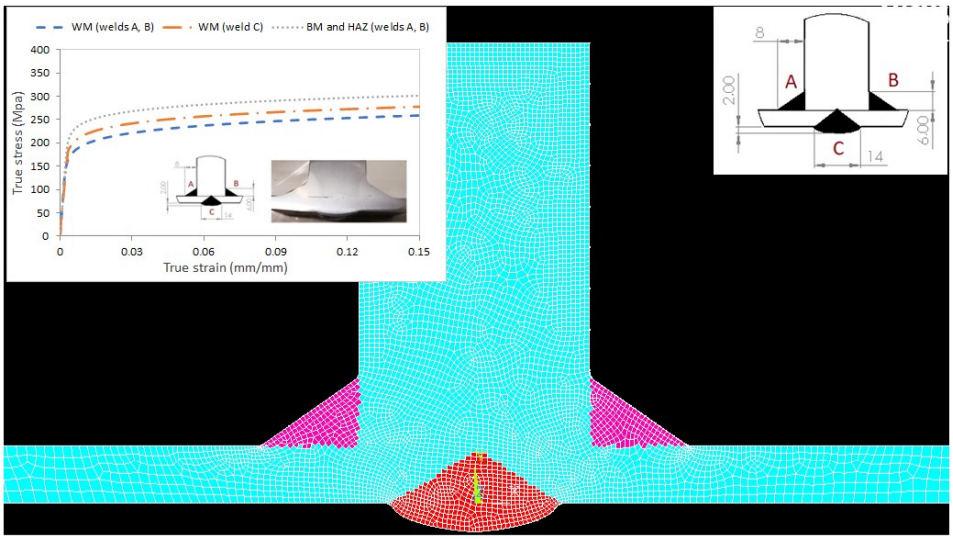

Figure 5. FE model and material curves.

The FEA results in terms of longitudinal strains are reported in Figure 6. The same strain scale of the DIC analysis (Figure 4) was used in order to compare results. The results clearly show the presence of strain due to bending (positive values close to 1%) at minimum applied displacement).

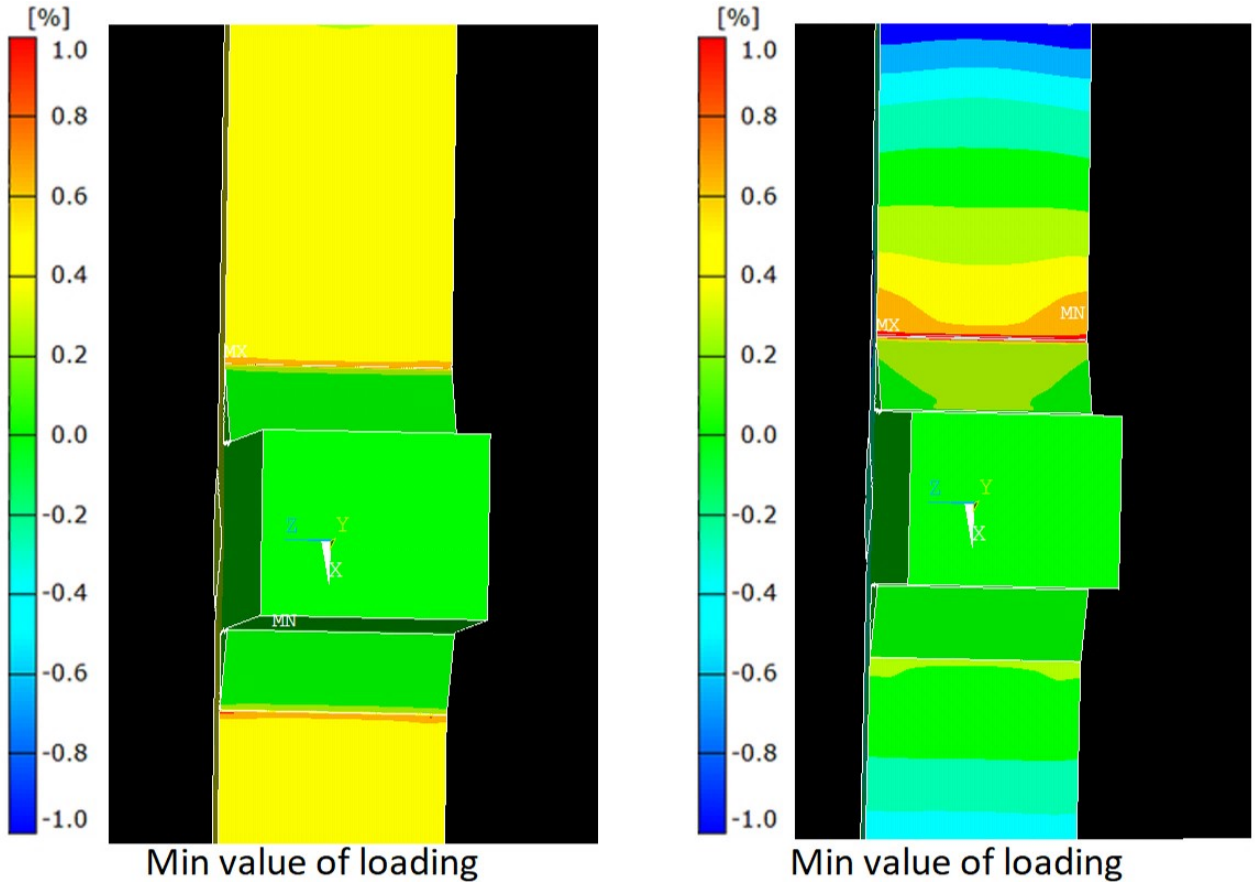

Figure 6. Longitudinal strain maps by means of FEA. ((**Left**) max value of loading; (**Right**) min value of loading.)

SP 4 was selected for further comparison between FE analysis and DIC analysis and is reported in Figure 7. The comparison is in agreement at maximum and minimum strain values, with differences among the intermediate values. These differences between the intermediate values probably arose since the onset of buckling is not immediate during displacement controlled experimental tests, therefore instability phenomena started, with less intensity, for lower values of applied displacement. However, both DIC and FE results indicated the onset of compression instability at a time of 0.85 s, which matches $d_a = -0.3$ mm with a strain change in sign. The effectiveness of the FE procedure and the displacement values for which buckling occurs were successfully verified.

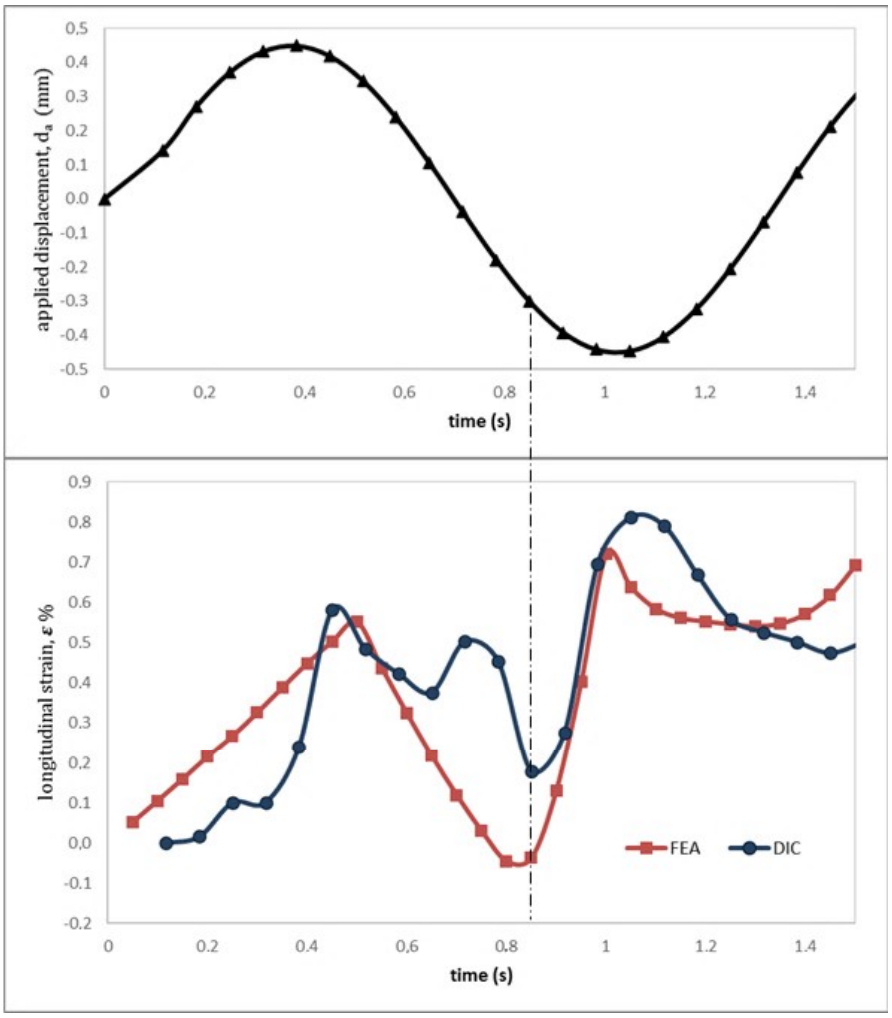

Figure 7. Strain values comparison between FEA and DIC.

4. Results from Low-Cycle Fatigue Evaluations

Displacement controlled low-cycle fatigue tests were performed using two values of displacement ratio: $R_d = -1$ and $R_d = 0$. The tests were conducted with a frequency of 5 Hz.

4.1. Low Cycle Fatigue Tests at $R_d = 0$

Tests at the displacement ratio $R_d = 0$ were conducted in order to avoid compression instability effects. Table 5 reports the applied displacement amplitude (d_a) at the grips and the experimental number of cycles to failure (N_{f_exp}).

Table 5. Parameters and number pf cycles of LCF tests at $R_d = 0$.

Test	Displacement Amplitude d_a (mm)	Cycles to Failure N_{f_exp}
1	0.4	2350
2	0.5	850
3	0.45	1450
4	0.55	360
5	0.35	4050

The longitudinal strain at maximum and minimum values of displacement ($d_a = 0.35$ mm) is illustrated in Figure 8. The upper plate (displacement is applied from this plate) under-

goes higher strain values, but high strains also continue in the base materials and not only at the weld toes.

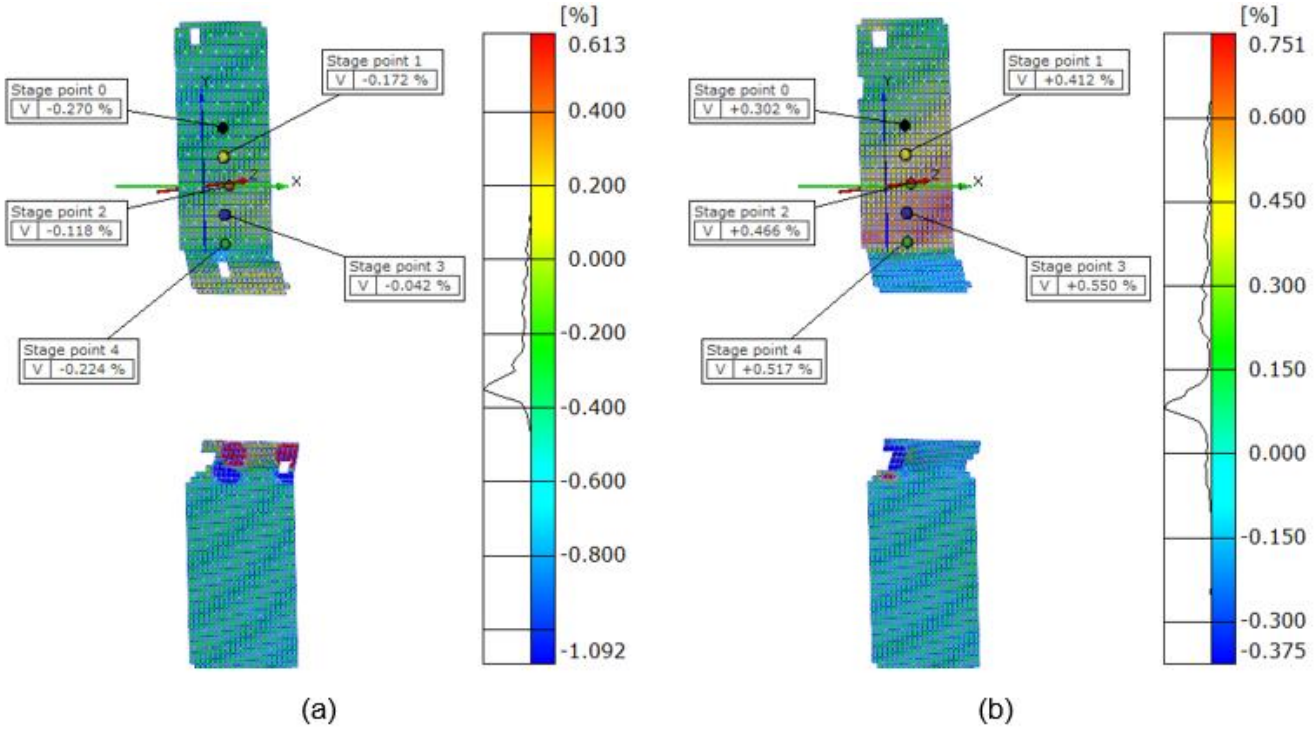

Figure 8. Longitudinal strain: (**a**) minimum value of displacement and (**b**) maximum value of displacement; (da = 0.35 mm).

Figure 9 shows the stabilized strain cycles of the Stage Points, showing an increment of the amplitude moving closer to the notch (SP4). The different Stage Points are "in-phase", meaning that no bending strains are detected at minimum applied displacement.

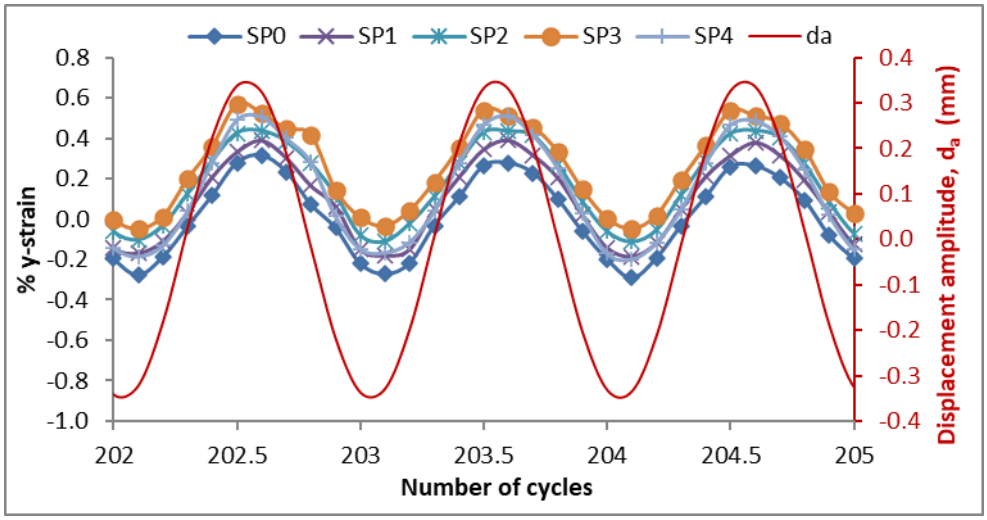

Figure 9. Longitudinal strain after 200 cycles; (d_a = 0.35 mm).

4.2. Low Cycle Fatigue Tests at $R_d = -1$

Fatigue tests at $R_d = -1$ at different amplitude displacement values were performed. Table 6 reports the displacement amplitude (d_a) and the number of cycles to failure (N_{f_exp}).

Table 6. LCF tests at $R_d = -1$.

Test	Displacement Amplitude d_a (mm)	Cycles to Failure N_{f_exp}
6	0.325	4500
7	0.35	2000
8	0.375	2900
9	0.4	1400
10	0.45	630
11	0.475	570
12	0.5	150

Figure 10 reports the strain map of the longitudinal component observed by the DIC cameras at maximum and minimum values of displacement. In contrast to what was observed for the tests at $R_d = -0$, from the figure it is possible to observe that in both cases the strain is positive near the welds, meaning that for compressive loading the specimens tend to deflect and tensile bending strains arise on the observed surface for the presence of buckling. Thus, one side (the toe fillet side that is in front of the cameras) is subjected to bending at positive values of strain, while the opposite side (the toe plate side) undergoes negative values (no cameras were placed on this side).

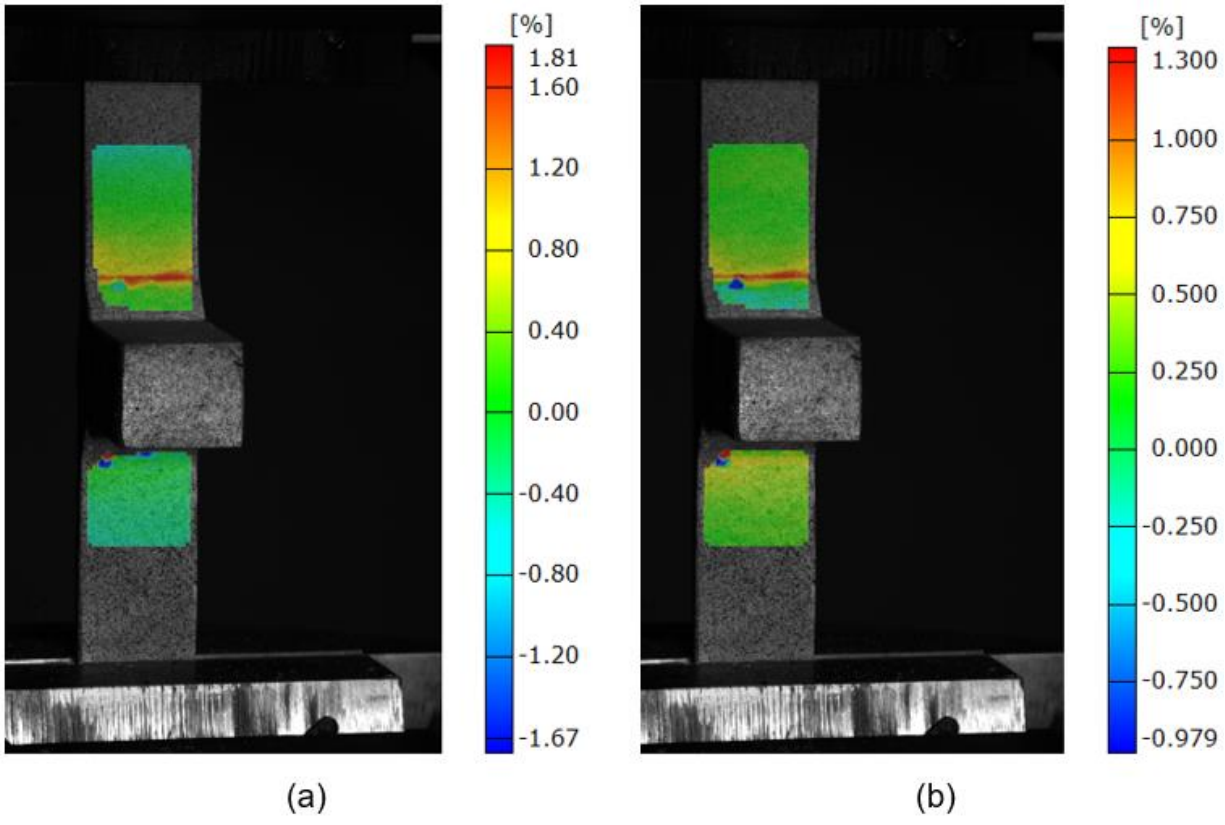

Figure 10. Longitudinal strain map: (**a**) minimum value of displacement and (**b**) maximum value of displacement; (d_a = 0.45 mm).

Figure 11 shows the longitudinal strain map at maximum and minimum values of displacement. From Figure 11a (d = −0.45 mm), it is possible to observe that the longitudinal strain is negative at the minimum applied displacement for SP0 (located at 20 mm from the weld notch) and becomes positive near the weld notch for the presence of buckling.

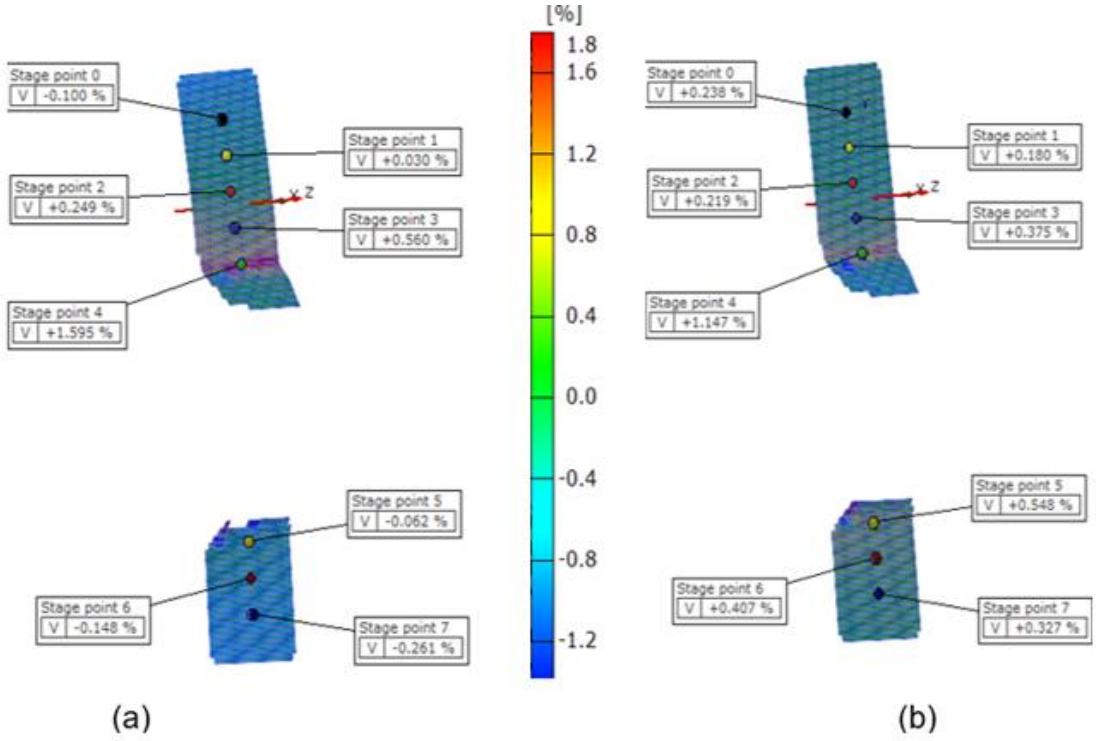

Figure 11. The 3D map and longitudinal strain of SP: (**a**) minimum value of displacement and (**b**) maximum value of displacement; (da = 0.45 mm).

This behaviour is further confirmed by Figure 12, which shows the evolution of the longitudinal strain (along y-axis shown in Figure 1) of the Stage Points after 200 cycles.

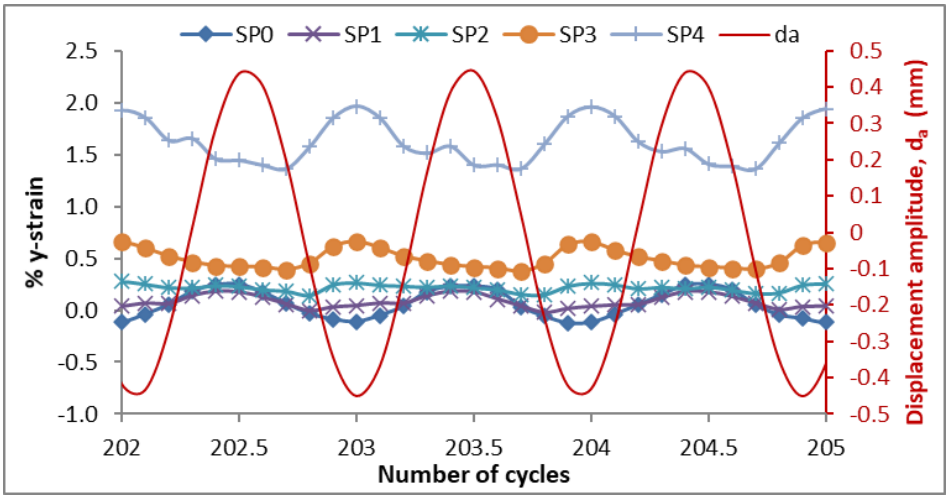

Figure 12. Longitudinal strain after 200 cycles; (d_a = 0.45 mm).

SP0, which is the furthest stage point from the weld toe, has negative strains at its minimum value of displacement and positive strains at its maximum displacement value. Moving closer to the weld toe, buckling phenomena increase for negative applied displacement values, producing positive strains with values of almost 1.9% at 1 mm close to the weld toe.

Figure 13 displays the obtained experimental curve $d_a - N$ at $R_d = 0$ and the comparison with the test at $R_d = -1$. Figure 13 shows that the tests at $R_d = 0$ follow longer fatigue lives than the data tests performed at $R_d = -1$, applying high values of displacement amplitudes ($d_a > 0.35$ mm). The results for $R_d = 0$ and $R_d = -1$ are indeed very close, only a

slight difference is noted in Figure 13 at low values of applied displacement ($d_a < 0.35$ mm), which means that no compression instability occurs. It is known that the effect of mean strain on strain range is neglectable for some cycles with N higher than 10 (as described in [42]). In addition, Zhang et al. [43] stated that the strain ratio effect on the mean stress is not meaningful for high strain ranges.

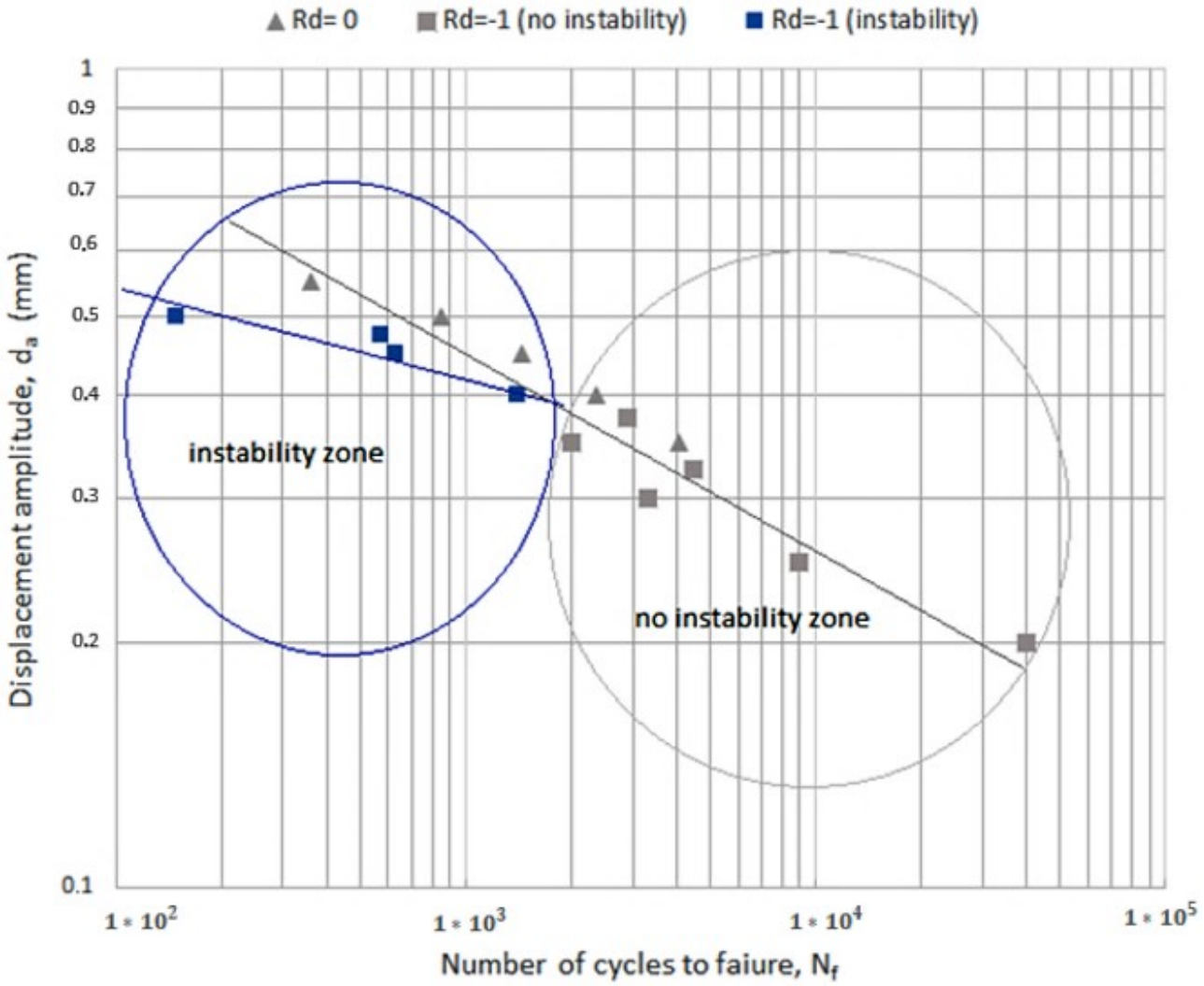

Figure 13. $d_a - N_f$ curve (results at $R_d = 0$ and $R_d = -1$).

If a difference must be noted, the contrary should be expected because the compressive loading is considered less dangerous on fatigue life, compared to tensile loading. Nevertheless, for the investigated welded joints, high compressive loading produced bending strains (as shown in Figure 12) and buckling, which significantly reduced the fatigue lives.

4.3. Finite Element Evaluation for LCF Analysis

A 3D FE model using the same parameters described for the static analysis was developed. The difference was due to the elastic-plastic material stress–strain curves for BM and WM used in the simulation, that are given in Figure 3 for the cyclic stress–strain behaviour representation.

Figure 14 illustrates the longitudinal strain, obtained by the FEA at maximum and minimum values of displacement. From the figure it is possible to observe that in both cases the strain is positive near the welds, meaning that for compressive loading the specimen tends to deflect, and tensile bending strains arise on the observed surface for the presence of

buckling. As previously observed, the onset of compression instability produces buckling-like deformations, thus the specimen undergoes bending with a strain change in sign (as shown in Figure 7).

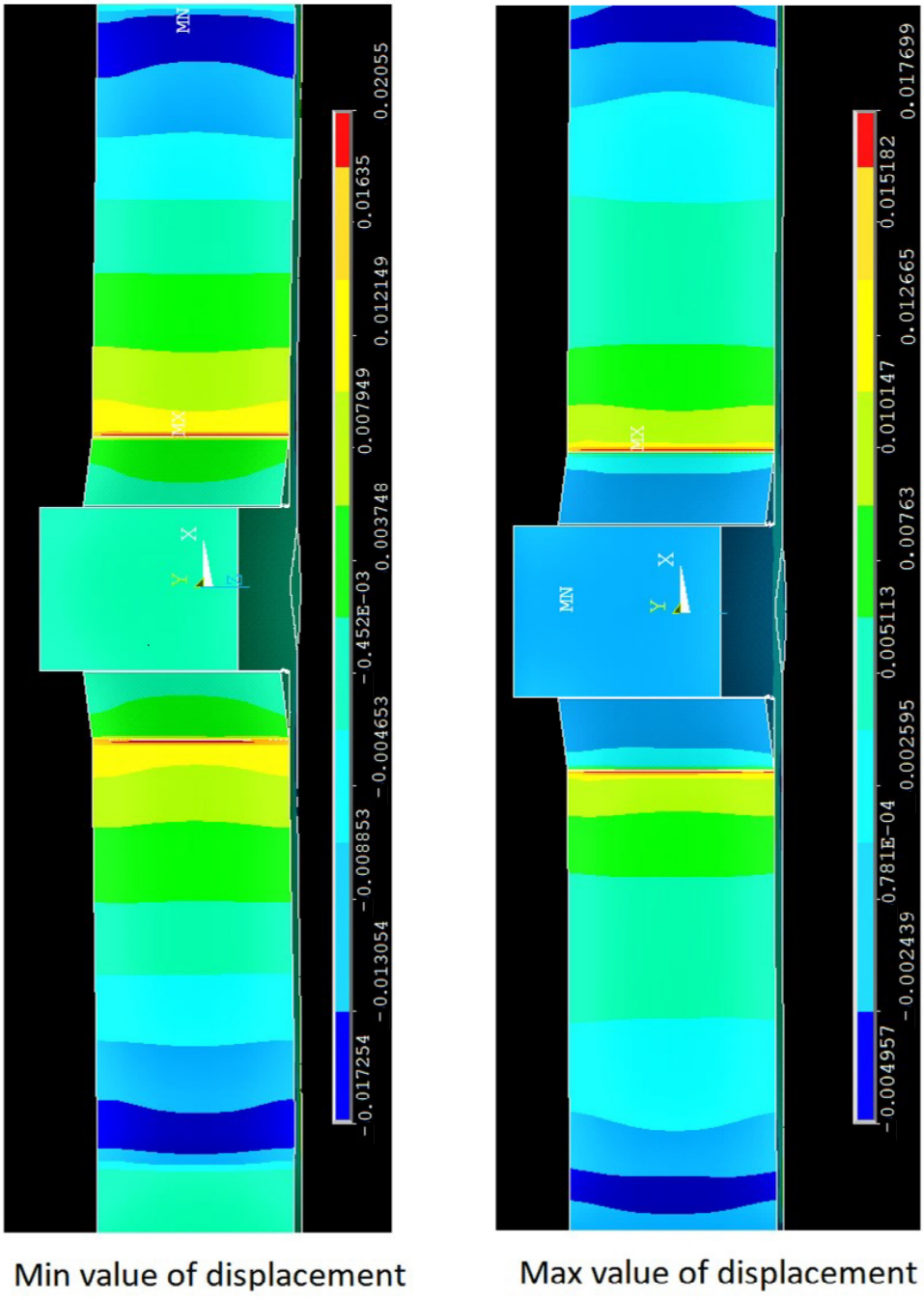

Figure 14. FE longitudinal strain map; ($d_a = \pm 0.45$ mm, $R_d = -1$). ((**Left**) min value of displacement; (**Right**) max value of displacement.)

The surface strains corresponding to the SP0 and SP4 positions were extracted from the FE model and compared with the DIC measurements shown in Figure 12. The comparison is provided in Figure 15. Given the uncertainty of the loading history, geometric condition (toe radius) and material properties, the comparison looks reasonable, which verifies both the FE model and the experimental measurements. The comparison further clarifies the positive peak surface strain around the weld toe at the SP4 location.

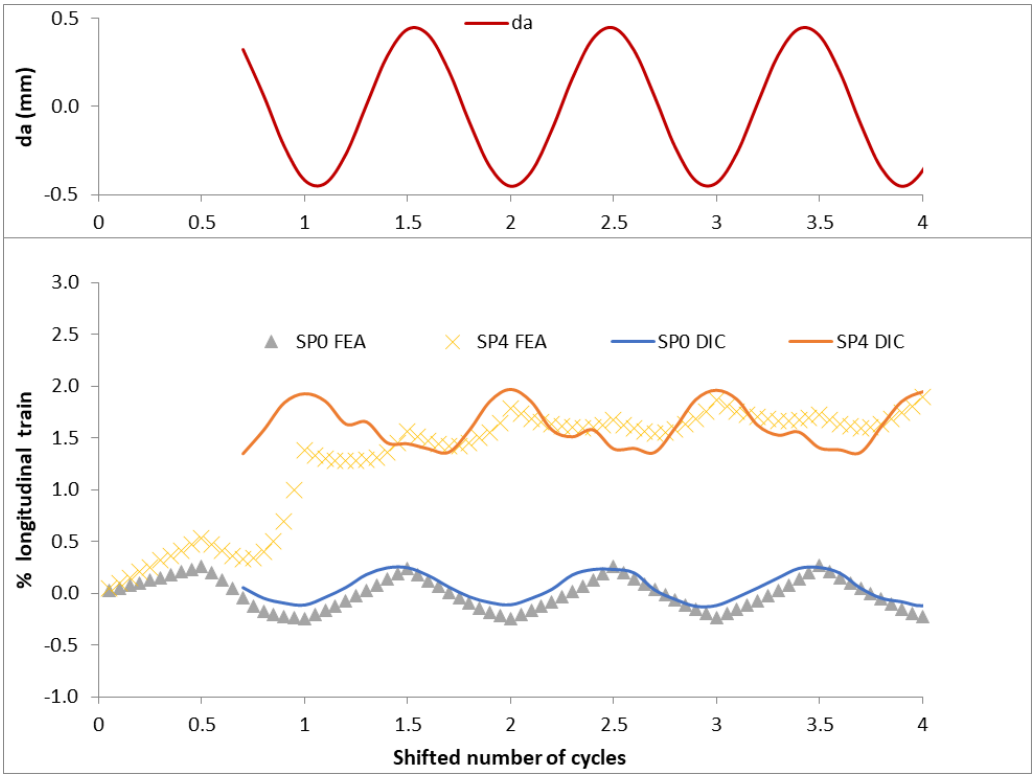

Figure 15. Surface strain at SP4 (near weld toe) and SP0; DIC (lines) vs. FEA (symbols) evaluation.

The procedure of calculating the different mechanical properties, both static and cyclic, from simple hardness measurements only, together with the effect of high values of applied displacement during the compression phase (and how these affect the LCF life), showed effectiveness when instability phenomena must be considered. This could help designers assess instability phenomena with a rapid calculation, in relation to causes that could produce significant fatigue loading.

5. Conclusions

LCF tests of welded joints made of AA 5083 used in marine environments were performed under displacement controls.

One preliminary static test was performed in order to detect the onset of buckling, in terms of applied displacement.

The curve in terms of displacement–number of cycles was evaluated and reveals that when applying high values of displacement amplitude ($d_a > 0.35$ mm), tests at $R_d = 0$ have longer fatigue lives than tests performed at $R_d = -1$. No influence of the different displacement ratios on the $d_a - N$ curve is observed at low values of the applied displacement ($d_a < 0.35$ mm).

The 3D analyses carried out by digital image correlation show that, for tests with a displacement ratio of minus one and $d_a > 0.35$ mm, strain is always positive near the welds, meaning that for compressive loads the specimen tends to buckle and bending arises.

A non-linear FE procedure to evaluate the elastic-plastic behaviour and the onset of compression instability was used. The procedure was based on simple hardness measurements that were used for the classification of the different mechanical properties of the zones (BM, and WM) and were applied in the nonlinear finite element model. This permits the simulation of complex non-linear phenomena starting only from values of hardness.

The procedure was validated experimentally by means of the DIC technique for displacement-controlled tests, effectively predicting the onset of compression instability.

As a general conclusion, the procedure of calculating the different mechanical properties, both static and cyclic, from simple hardness measurements only, has shown effectiveness when instability phenomena must be simulated, for both static and LCF conditions.

Funding: This research received no external funding.

Acknowledgments: The research reported in this paper was conducted in the facilities of the Research Project "CERISI" ("Research and Innovation Centre of Excellence for Structure and Infrastructure of Large Dimensions") and funded by the PON (National Operative Programme) 2007–2013.

Conflicts of Interest: The author declares no conflict of interest.

References

1. Mei, X.; Xiong, M. Effects of second-order hydrodynamics on the dynamic responses and fatigue damage of a 15 mw floating offshore wind turbine. *J. Mar. Sci. Eng.* **2021**, *9*, 1232. [CrossRef]
2. Yang, Q.; Li, G.; Mu, W.; Liu, G.; Sun, H. Identification of crack length and angle at the center weld seam of offshore platforms using a neural network approach. *J. Mar. Sci. Eng.* **2020**, *8*, 40. [CrossRef]
3. Hirdaris, S.E.; Bai, W.; Dessi, D.; Ergin, A.; Gu, X.; Hermundstad, O.A.; Huijsmans, R.; Iijima, K.; Nielsen, U.D.; Parunov, J.; et al. Loads for use in the design of ships and offshore structures. *Ocean Eng.* **2014**, *78*, 131–174. [CrossRef]
4. Pinheiro, B.d.C.; Pasqualino, I.P. Fatigue analysis of damaged steel pipelines under cyclic internal pressure. *Int. J. Fatigue* **2009**, *31*, 962–973. [CrossRef]
5. Erny, C.; Thevenet, D.; Cognard, J.Y.; Körner, M. Fatigue life prediction of welded ship details. *Mar. Struct.* **2012**, *25*, 13–32. [CrossRef]
6. Feng, L.; Qian, X. Low cycle fatigue test and enhanced lifetime estimation of high-strength steel S550 under different strain ratios. *Mar. Struct.* **2018**, *61*, 343–360. [CrossRef]
7. Syed Ahmad, S.Z.A.; Abu Husain, M.K.; Mohd Zaki, N.I.; Mukhlas, N.A.; Mat Soom, E.; Azman, N.U.; Najafian, G. Offshore Structural Reliability Assessment by Probabilistic Procedures—A Review. *J. Mar. Sci. Eng.* **2021**, *9*, 998. [CrossRef]
8. ASM Handbook Volume 6: Welding, Brazing, and Soldering—ASM International. Available online: https://www.asminternational.org/search/-/journal_content/56/10192/06480G/PUBLICATION (accessed on 26 February 2021).
9. Zhao, W.; Hsu, W.T. Re-evaluation of fatigue thickness effect based on fatigue test database. *J. Mar. Sci. Eng.* **2020**, *8*, 895. [CrossRef]
10. Liao, X.; Qiang, B.; Wu, J.; Yao, C.; Wei, X.; Li, Y. An improved life prediction model of corrosion fatigue for T-welded joint. *Int. J. Fatigue* **2021**, *152*, 106438. [CrossRef]
11. Fricke, W. Recent developments and future challenges in fatigue strength assessment of welded joints. *Proc. Inst. Mech. Eng. Part C J. Mech. Eng. Sci.* **2015**, *229*, 1224–1239. [CrossRef]
12. Radaj, D.; Sonsino, C.M.; Fricke, W. Recent developments in local concepts of fatigue assessment of welded joints. *Int. J. Fatigue* **2009**, *31*, 2–11. [CrossRef]
13. Dong, P. A structural stress definition and numerical implementation for fatigue analysis of welded joints. *Int. J. Fatigue* **2001**, *23*, 865–876. [CrossRef]
14. Radaj, D.; Sonsino, C.M.; Fricke, W. *Fatigue Assessment of Welded Joints by Local Approaches*, 2nd ed.; Elsevier: Amsterdam, The Netherlands, 2006; ISBN 9781855739482.
15. Sonsino, C.M.; Radaj, D.; Brandt, U.; Lehrke, H.P. Fatigue assessment of welded joints in AlMg 4.5Mn aluminum alloy (AA 5083) by local approaches. *Int. J. Fatigue* **1999**, *21*, 985–999. [CrossRef]
16. Lazzarin, P.; Tovo, R. A notch intensity factor approach to the stress analysis of welds. *Fatigue Fract. Eng. Mater. Struct.* **1998**, *21*, 1089–1103. [CrossRef]
17. Atzori, B.; Lazzarin, P.; Meneghetti, G.; Ricotta, M. Fatigue design of complex welded structures. *Int. J. Fatigue* **2009**, *31*, 59–69. [CrossRef]
18. Taylor, D.; Barrett, N.; Lucano, G. Some new methods for predicting fatigue in welded joints. *Int. J. Fatigue* **2002**, *24*, 509–518. [CrossRef]
19. Taylor, D. *The Theory of Critical Distances: A New Perspective in Fracture Mechanics*; Elsevier: Amsterdam, The Netherlands, 2007; ISBN 9780080554723.
20. Fan, J.L.; Guo, X.L.; Wu, C.W.; Zhao, Y.G. Research on fatigue behavior evaluation and fatigue fracture mechanisms of cruciform welded joints. *Mater. Sci. Eng. A* **2011**, *528*, 8417–8427. [CrossRef]
21. Williams, P.; Liakat, M.; Khonsari, M.M.; Kabir, O.M. A thermographic method for remaining fatigue life prediction of welded joints. *Mater. Des.* **2013**, *51*, 916–923. [CrossRef]
22. Wang, X.G.; Crupi, V.; Jiang, C.; Guglielmino, E. Quantitative Thermographic Methodology for fatigue life assessment in a multiscale energy dissipation framework. *Int. J. Fatigue* **2015**, *81*, 249–256. [CrossRef]
23. Corigliano, P.; Crupi, V. Fatigue analysis of TI6AL4V/INCONEL 625 dissimilar welded joints. *Ocean Eng.* **2021**, *221*, 108582. [CrossRef]

24. Saiprasertkit, K. Fatigue strength assessment of load-carrying cruciform joints in low- and high-cycle fatigue region based on effective notch strain concept: HENRY GRANJON PRIZE 2013 Winner Category C: Design and Structural Integrity. *Weld. World* **2014**, *58*, 455–467. [CrossRef]
25. Dong, P.; Pei, X.; Xing, S.; Kim, M.H. A structural strain method for low-cycle fatigue evaluation of welded components. *Int. J. Press. Vessel. Pip.* **2014**, *119*, 39–51. [CrossRef]
26. Hobbacher, A. *Recommendations for Fatigue Design of Welded Joints and Components*; IIW Doc. IIW-1823-07 ex XIII-2151r4-07/XV-1254r4-07; International Institute of Welding: Paris, France, 2008.
27. Dong, P.; Prager, M.; Osage, D.A.; Hong, J.K.; Dewees, D.J. *The Master S-N Curve Method: An Implementation for Fatigue Evaluation of Welded Components in the ASME B & PV Code, Section VIII, Division 2 and API 579-1/ASME FFS-1*; Welding Research Council: New York, NY, USA, 2010; ISBN 9781581455304.
28. Pei, X.; Dong, P.; Xing, S. A structural strain parameter for a unified treatment of fatigue behaviors of welded components. *Int. J. Fatigue* **2019**, *124*, 444–460. [CrossRef]
29. Pei, X.; Dong, P. An analytically formulated structural strain method for fatigue evaluation of welded components incorporating nonlinear hardening effects. *Fatigue Fract. Eng. Mater. Struct.* **2019**, *42*, 239–255. [CrossRef]
30. Xing, R.; Yu, D.; Shi, S.; Chen, X. Cyclic deformation of 316L stainless steel and constitutive modeling under non-proportional variable loading path. *Int. J. Plast.* **2019**, *120*, 127–146. [CrossRef]
31. Su, M.; Xu, L.; Peng, C.; Han, Y.; Zhao, L. Fatigue short crack growth, model and EBSD characterization of marine steel welding joint. *Int. J. Fatigue* **2022**, *156*, 106689. [CrossRef]
32. Corigliano, P.; Crupi, V.; Guglielmino, E. Non linear finite element simulation of explosive welded joints of dissimilar metals for shipbuilding applications. *Ocean Eng.* **2018**, *160*, 346–353. [CrossRef]
33. Corigliano, P.; Crupi, V.; Pei, X.; Dong, P. DIC-based structural strain approach for low-cycle fatigue assessment of AA 5083 welded joints. *Theor. Appl. Fract. Mech.* **2021**, *116*, 103090. [CrossRef]
34. Corigliano, P.; Ragni, M.; Castagnetti, D.; Crupi, V.; Dragoni, E.; Guglielmino, E. Measuring the static shear strength of anaerobic adhesives in finite thickness under high pressure. *J. Adhes.* **2019**, *98*, 783–800. [CrossRef]
35. GOM mbH. *ARAMIS User Manual—Software V6.3.*; GOM mbH: Braunschweig, Germany, 2011; pp. 1–129.
36. Atzori, B.; Meneghetti, G. Fatigue strength of fillet welded structural steels: Finite elements, strain gauges and reality. *Int. J. Fatigue* **2001**, *23*, 713–721. [CrossRef]
37. Fricke, W. *IIW Recommendations for the Fatigue Assessment of Welded Structures by Notch Stress Analysis: IIW-2006-09*; Woodhead Publishing: Sawston, UK, 2012; ISBN 9780857098559.
38. Stathers, P.A.; Hellier, A.K.; Harrison, R.P.; Ripley, M.I.; Norrish, J. Hardness–Tensile Property Relationships for HAZ in 6061-T651 aluminum. *Weld. J.* **2014**, *93*, 301–311.
39. Kamaya, M. Ramberg–Osgood type stress–strain curve estimation using yield and ultimate strengths for failure assessments. *Int. J. Press. Vessel. Pip.* **2016**, *137*, 1–12. [CrossRef]
40. Lopez, Z.; Fatemi, A. A method of predicting cyclic stress-strain curve from tensile properties for steels. *Mater. Sci. Eng. A* **2012**, *556*, 540–550. [CrossRef]
41. Niu, P.; Li, W.; Chen, Y.; Liu, F.; Gong, J.; Chen, D. Cyclic hardening behavior and deformation mechanisms of friction-stir-welded dissimilar AA5083-to-AA2024 joints with heterogeneous microstructures. *Mater. Charact.* **2021**, *181*, 111465. [CrossRef]
42. Ohji, K.; Miller, W.R.; Marin, J. Cumulative damage and effect of mean strain in low-cycle fatigue of a 2024-T351 aluminum alloy. *J. Basic Eng.* **1966**, *88*, 801–809. [CrossRef]
43. Zhang, J.; Li, W.; Dai, H.; Liu, N.; Lin, J. Study on the elastic-plastic correlation of low-cycle fatigue for variable asymmetric loadings. *Materials* **2020**, *13*, 2451. [CrossRef]